Sunlight-absorbing aerosol amplifies the seasonal cycle in low cloud fraction over the southeast Atlantic

Jianhao Zhang[1] and Paquita Zuidema[2]

[1]Chemical Sciences Laboratory, NOAA Earth System Research Laboratories, Boulder, CO, USA
[2]Rosenstiel School of Marine and Atmospheric Sciences, University of Miami, Miami, FL, USA

Correspondence: Jianhao Zhang (jzhang@miami.edu)

Abstract. Many studies examining shortwave-absorbing aerosol-cloud interactions over the southeast Atlantic apply a seasonal averaging. This disregards a meteorology that raises the mean altitude of the smoke layer from July to October. This study details the month-by-month changes in cloud properties and the large-scale environment as a function of the biomass-burning aerosol loading at Ascension Island from July to October, based on measurements from Ascension Island (8°S, 14.5°W), satellite retrievals and reanalysis. In July and August, variability in the smoke loading predominantly occurs in the boundary layer. During both months, the low-cloud fraction is less and is increasingly cumuliform when more smoke is present, with the exception of a late morning boundary layer deepening that encourages a short-lived cloud development. The meteorology varies little, suggesting aerosol-cloud interactions consistent with a boundary-layer semi-direct effect can explain the cloudiness changes. September marks a transition month during which mid-latitude disturbances can intrude into the Atlantic subtropics, constraining the land-based anticyclonic circulation transporting free-tropospheric aerosol to closer to the coast. Stronger boundary layer winds help deepen, dry, and cool the boundary layer near the main stratocumulus deck compared to that on days with high smoke loadings, with stratocumulus reducing everywhere but at the northern deck edge. Longwave cooling rates generated by a sharp water vapor gradient at the aerosol layer top facilitates small-scale vertical mixing, and could help to maintain a better-mixed September free troposphere. The October meteorology is more singularly dependent on the strength of the free-tropospheric winds advecting aerosol offshore. Free-tropospheric aerosol is less, and moisture variability more, compared to September. Low-level clouds increase and are more stratiform, when the smoke loadings are higher. The increased free-tropospheric moisture can help sustain the clouds through reducing evaporative drying during cloud-top entrainment. Enhanced subsidence above the coastal upwelling region increasing cloud droplet number concentrations may further prolong cloud lifetime through microphysical interactions. Reduced subsidence underneath stronger free-tropospheric winds at Ascension supports slightly higher cloud tops during smokier conditions. Overall the monthly changes in the large-scale aerosol and moisture vertical structure act to amplify the seasonal cycle in low-cloud amount and morphology, raising a climate importance as cloudiness changes dominate changes in the top-of-atmosphere radiation budget.

1   Introduction

25   The impact of absorbing aerosol on marine boundary layer clouds is sensitive most importantly to the relative location of the aerosol layer to the cloud layer, with aerosol embedded within the cloud layer giving rise to local aerosol-cloud microphysical interactions, while aerosol above a cloud layer is only active radiatively until it is entrained into the cloud (Johnson et al., 2004; Johnson, 2005; Costantino and Bréon, 2013; Yamaguchi et al., 2015; Zhou et al., 2017; Zhang and Zuidema, 2019; Kacarab et al., 2020; Herbert et al., 2020). Many studies focusing on the southeast Atlantic region apply a seasonal-averaging to improve

30   the robust detection of absorbing aerosol impacts (e.g., Wilcox, 2010, 2012; Adebiyi and Zuidema, 2018; Mallet et al., 2020). This neglects a noticeable rise in the smoke layer, from mostly within the boundary layer in July (Zuidema et al., 2018), to a mixture of boundary layer and free-tropospheric smoke in August (Zhang and Zuidema, 2019; Redemann et al., 2021; Haywood et al., 2021), to mostly above and distinctly separated from the cloud layer by September and October (Shinozuka et al., 2020; Redemann et al., 2021; Haywood et al., 2021).

35   Zhang and Zuidema (2019, hereafter ZZ19) characterized the diurnal behavior of low-clouds and boundary layer thermodynamic structures as a function of the smoke loading during August over Ascension Island (8° S, 14.5° W) in the remote southeast Atlantic. This was motivated by the observation that the near-surface refractory black carbon (rBC) mass concentration measurements were largest during August, based on measurements from two years gathered through the Layered Atlantic Smoke Interactions with Clouds (LASIC; Zuidema et al., 2015, 2018) campaign. Furthermore, when more smoke is present

40   within the marine boundary layer (MBL), low clouds are fewer, with lower liquid water paths and lower precipitation frequencies and intensities, compared to clouds occupying a cleaner MBL. The reduction in cloudiness, which often spans multiple days, is consistent with a boundary layer semi-direct effect (Ackerman et al., 2000), wherein the relative humidity is reduced within a warmer boundary layer and less able to sustain cloud. The August analyses also support a novel finding in which the boundary layer is more coupled in the late morning (after sunrise) under smokier conditions, facilitating the cloud vertical de-

45   velopment and deepening the boundary layer. Boundary layer decoupling from afternoon to pre-dawn encourages the trapping of sub-cloud moisture that is then ventilated upwards in the morning. This coupling is short-lived, with most of the cloudiness reduction occurring in the afternoon.

Here we build on ZZ19 and extend the analyses to the other months containing biomass-burning aerosol within the southeast Atlantic atmosphere (July–October). Already known is that the free-tropospheric transport of smoke to the remote part of the

50   southeast Atlantic is related to variability in the strength of the southern African Easterly Jet (AEJ-S; Adebiyi and Zuidema, 2016) during primarily September-October, and that the AEJ-S can also advect water vapor (Adebiyi et al., 2015; Deaconu et al., 2019; Pistone et al., 2021). The meteorology governing aerosol transport in July-August is less well-known, although case studies indicate lower-level easterlies bring aerosol in closer contact with the cloud layer then, easing entrainment (Zuidema et al., 2018; Diamond et al., 2018). Also less well-known, is how the cloud properties could be influenced by the meteorology

55   governing the aerosol transport, and to the co-varying moisture loading, as well as how significantly synoptic variability could be imprinting into possible aerosol-cloud interactions, at synoptic time scales. Although these questions are not new, new

datasets, in particular the unique island-based LASIC field measurements, provide more detailed characterizations capable of providing new insights, than were possible prior to 2016.

This study characterizes the sub-seasonal evolution in low-clouds and thermodynamic structures as a function of the aerosol loading from July-October of 2016 and 2017. In so doing it combines the LASIC field measurements with space-based retrievals of aerosol and low-cloud properties that can distinguish the above-cloud aerosol optical depth (Meyer et al., 2015), and the newer ERA5 reanalysis, which is known to provide a more accurate depiction of the vertical moisture distribution (Pistone et al., 2021). Compositing methods and datasets are introduced in Section 2. Sections 3-6 present an overview of the seasonal cycle, as well as the observed differences by month for high and low smoke loading. Section 7 illustrates how a sharp water vapor gradient can promote small-scale vertical mixing in the free-tropospheric aerosol layer. Section 8 summarizes the key findings.

2 Datasets and compositing approach

Ground-based measurements were collected by the Department of Energy (DOE) Atmospheric Radiation Measurement (ARM) Mobile Facility 1 (AMF1; Miller et al., 2016). Radiosonde measurements of temperature, water vapor mixing ratio (q_v), relative humidity and wind characterize the thermodynamic and dynamic vertical structure above Ascension Island and St. Helena Island (5° W, 15° S, upwind of Ascension). A Ka-band 35 GHz zenith-pointing cloud radar (KAZR) provides a diurnal cycle of the cloud vertical structure. Microwave radiometers at both the AMF1 site and the airport (∼5 km away from the AMF1) provide a measure of the cloud liquid water path (LWP). Surface rain frequencies and intensities were measured by a disdrometer and a tipping bucket at the AMF1 site. No radar or disdrometer data are available for October, 2017. The near-surface rBC mass concentrations were derived from a single-particle soot photometer (SP2). A micro-pulse lidar provided vertically resolved extinction profiles (Delgadillo et al., 2018) for the radiative transfer calculations. Surface observers from the United Kingdom's Meteorological Office at Ascension Island, trained to look away from the island, reported cloud types following the World Meteorological Organization protocol (WMO, 1974) every 3 hours. Detailed descriptions of LASIC observations, including quality control and post-processing information, can be found in Section 2 of ZZ19.

The MODerate resolution Imaging Spectroradiometer (MODIS) on board Terra and Aqua satellites supported Collection 6 retrievals of liquid-cloud properties (Platnick et al., 2003) and fine-mode aerosol optical depth at 550 nm (τ_{af}; Levy et al., 2013) at 1° resolution (Level-3), chosen to exclude contributions from large aerosol particles, e.g. sea salt. Above-cloud aerosol optical depth at 550 nm (ACAOD) from the same platforms, at 0.1° resolution, are available from Meyer et al. (2015, hereafter MODIS-Meyer). Cloud droplet number concentrations (N_d) are calculated based on cloud effective radius (r_e) and cloud optical thickness (τ_{cld}) from the MODIS-Meyer product, following Painemal and Zuidema (2011). MODIS-Meyer cloud and aerosol retrievals are aggregated to 1° resolution to match the level-3 MODIS retrievals, if the former can provide an areal coverage of at least 20%. Daily-mean values of these MODIS-based retrievals over Ascension rely on averages between the daily Terra and Aqua overpasses weighted by their retrieval counts, and are then averaged spatially over 2° by 2°, 3° by 3°, and 4° by 4° domains centered on Ascension. Low-cloud fractions across the diurnal cycle are retrieved using the Visible Infrared

Solar-Infrared Split Window Technique (VISST; Minnis et al., 2008) from the Spinning Enhanced Visible and Infrared Imager (SEVIRI) on board the geostationary Meteosat10 satellite. These are averaged over a 4° by 4° domain latitudinally centered on Ascension but with a longitudinal center slightly to the island's east (6-10° S, 15-11° W), thought to better capture the upwind clouds more typical of the island. All-sky albedos at the top-of-atmosphere (TOA) are calculated as the ratio between reflected shortwave fluxes at TOA and the incoming solar radiation measured by the Clouds and the Earth's Radiant Energy Systems (CERES; Wielicki et al., 1996) sensor onboard Terra and Aqua satellites. CERES Single Scanner Footprint (resolution of 20 km) product Edition 4 (Su et al., 2015) is used for these calculations.

Meteorological conditions (geopotential heights, temperatures and wind velocities) are inferred from the European Centre for Medium-Range Weather Forecasts (ECMWF) fifth-generation atmospheric reanalysis (ERA5; Hersbach et al., 2020), available every hour and gridded to 0.25° spatial resolution. Back trajectories from Ascension Island at 2000 m, or just above the cloud tops, help indicate the transport of aerosol most likely to entrain into the boundary layer near Ascension. The back trajectories rely on the NOAA Hybrid Single-Particle Lagrangian Integrated Trajectory (HYSPLIT; Draxler and Hess, 1998) model, initialized by the NOAA National Center for Environmental Prediction (NCEP) Global Data Assimilation System (GDAS) at 0.5° spatial resolution and relying on the model vertical velocity. Radiative transfer calculations rely on the Atmospheric and Environmental Research Rapid Radiative Transfer Model for GCMs (RRTMG; Clough et al., 2005), using version 4.84 of the longwave (LW) code and version 3.8 of the shortwave (SW) code.

The basic approach is to construct composites of those conditions deemed more or less smoky for each month, and to analyze the differences in cloud properties with an eye on the accompanying meteorology as well as aerosol. A difficulty rests with what to call smoky in each month: surface-based measurements may not be indicative of the free-tropospheric aerosol loading and vice versa. Joint histograms of daily ACAOD and rBC mass concentrations over Ascension, by month, indicate that smoke is predominantly present in the boundary layer during July, equally frequent in the boundary layer and free-troposphere in August, and mostly in the free troposphere in September and October (Fig. 1). Yet, ACAOD is only available when there is cloud underneath (Meyer et al., 2015), allowing free-tropospheric smoke in clear conditions to go undetected. This bias is most likely (potentially) in July, when the low cloud fraction is lower (ZZ19). To reduce this bias, the daily-mean τ_{af} was also examined. These are not entirely interchangeable (a correlation of $\sim$0.55 over 3° by 3° domain-average in September and October, with a clear bias between the two measures; Fig. 1, right), but these do provide two independent pieces of information. In addition, 3-day running-means (Fig. 2a) and visual inspections of spatial maps of ACAOD and τ_{af} aim to ensure that the classification of days as more/less smoky was representative of the larger region around Ascension. For September and October, when most of the smoke is above the low cloud deck, daily-mean values of τ_{af} and ACAOD over Ascension mostly rely on 2° by 2° domain-averages, but averages over 3° by 3° and 4° by 4° regions supplement this when information over the smaller domain is limited.

During July–August, column τ_{af} mostly tracks near-surface rBC concentrations, except for a few days in early July 2016 (Fig. 2a). Only a few days with high ACAOD are identified, with those in 2017 coinciding with high rBC mass concentrations near the surface (not so in early July 2016). This suggests that the use of the surface-based rBC values is a reasonable indicator of the total column aerosol loading, most of the time, in July. In August, ACAOD and τ_{af} track each other well, and, interest-

125 ingly, appear to anticipate the high near-surface smoke loadings by up to a week. For August, composite decisions primarily follow those of ZZ19, and the behavior of those time periods with increased free-tropospheric smoke loadings prior, is left to a further study. In September and October, τ_{af} tracks ACAOD fairly well, with τ_{af} confirming that those days with missing ACAODs indeed correspond to days with little free-tropospheric aerosol (e.g., early September 2016, 2nd week of October 2016). The evolution in the smoke vertical distribution is consistent with that from space-based lidar observations (Redemann

130 et al., 2021) and surface observations (Fig. 2a).

The implemented approach is to use thresholds to indicate more/less smoky conditions for each month based approximately on the tercile values of the daily-mean rBC mass concentrations in July and August, similar to ZZ19. The thresholds for September and October rely first on the daily-mean MODIS-retrieved τ_{af} values, because these vary more smoothly with time than do the ACAOD values, and secondarily on the ACAOD values. No attempt is made to account for the bias between the τ_{af}

135 and ACAOD values (Fig. 1, right panel), with the ACAOD values primarily used as a sanity check on τ_{af}. Threshold values also account for differences in biomass burning activity between the months, and are relaxed to whole numbers for ease of readership. The thresholds applied are: rBC mass concentrations of 100 and 400 ng m^{-3}, respectively, for low and high smoke loadings in the boundary layer in July; 100 increasing to 500 ng m^{-3} for the smokier month of August. In September, optical depths of 0.15 and 0.26, respectively, indicate low and high smoke loadings, reducing to 0.11 and 0.19 for the less smoky month

140 of October. These thresholds lead to 10 (25) days are selected for the high (low) smoke loading composite for July, 13 (13) for August, 19 (16) for September, and 19 (13) for October, from the two years combined. Ultimately, the use of composites is intended to prevent unique time periods from dominating perceptions of aerosol-cloud interaction behavior. Instead, composites can provide more statistically robust interpretations than can be gleaned from case studies alone. An example is the time period from early July, 2016, in which a time period with relatively high satellite-derived optical depths is classified as "less smoky"

145 based on the surface rBC values. For this particular time period, the classification is not completely correct. Nevertheless, the composite will be dominated by those days for which the full atmospheric column is truly clean (e.g., early July 2017).

3 July-October overview

The boundary layer cools, shoals, and moistens over Ascension from July to October (Fig. 2b), with the free troposphere warming more quickly than the surface, increasing the lower tropospheric stability from July to October (Fig. 2b). The boundary

150 layer is also most likely to be decoupled in July, although the mean thermodynamic profiles indicate some decoupling between the sub-cloud and cloud layer for all four months. The free-tropospheric wind speeds increase from July to October (Fig. 2). These are primarily easterly winds above 2 km and affect the timing of free-tropospheric smoke arriving above Ascension. The easterly wind episodes become more frequent in August (Fig. 2a). In September, the amount of smoke in the boundary layer reduces abruptly. In October, as convection moves southward over the African continent and biomass-burning activity

155 reduces (Adebiyi et al., 2015; Redemann et al., 2021), less smoke is present both below and above the low clouds, despite continuing strong easterlies, reflecting the southward movement of convection. In September and October, the "more smoky" periods correlate with the strength of the 2-4 km easterlies (Fig. 2a), reflecting the critical role of the free-tropospheric zonal jet

in transporting biomass-burning smoke over the remote ocean in austral spring. The August-September transitions in synoptic regimes occur earlier in 2016 than 2017, evident in the time series of the shifts in the various aerosol measures (Fig. 2a), and
160   consistent with larger-scale spatial distributions (Redemann et al., 2021). The UK Clouds and Aerosol Radiative Impacts and Forcing (CLARIFY) aircraft deployment from Ascension (Haywood et al., 2021) occurred from late August to mid-September, 2017, capturing the full range of aerosol-cloud vertical co-locations.

Consistent with the strengthening and lowering of the trade-wind temperature inversion from July to October (Fig. 2b), the satellite-derived low-cloud cover increases around Ascension from July to October (Fig. 3a), regardless of the smoke loading.
165   Stratiform clouds become more common, and cumuliform clouds less so (Fig. 3b). The boundary layer flow at Ascension is slightly downstream of the main southeast Atlantic stratocumulus region ($10°E – 0°E$, $10°S – 20°S$ as per Klein and Hartmann, 1993) and the gross aspects of the seasonal cycle in low cloud fraction and properties at Ascension appear similarly governed by large-scale meteorological parameters (Fuchs et al., 2017; Scott et al., 2020).

The striking feature of Fig. 3 is that when more absorbing aerosol is present over the remote southeast Atlantic, the seasonal
170   cycle in low-level cloudiness and cloud morphology becomes amplified. The low-cloud fraction reduces in July and August, favoring more cumuliform and less stratiform, whereas in October, the low-cloud cover increases, with stratiform clouds occurring more frequently, compared to a cleaner condition (Fig. 3). The amplitude of the diurnal cycle (Fig. 3a) is mostly unaffected by the smoke loading, except in August, when a more pronounced diurnal amplitude can be related to the afternoon clearing of stratiform clouds under smokier conditions (ZZ19). Overall the modulation of the cloudiness seasonal cycle by
175   the presence (or lack of) smoke is important because the cloudiness changes ultimately dominate the change to the top-of-atmosphere shortwave radiation balance (Fig. 3c). The all-sky albedo can either decrease or increase, depending to first order on the changes in the cloudiness fraction. This in turn depends on the relative location of the aerosols and clouds, reinforcing the need to better characterize the responsible processes (e.g., Che et al., 2021).

4   Cloud reduction in July

180   In July, when more smoke is present in the boundary layer (BL), low-cloud is less frequent throughout the day (Fig. 4a). Cloud based are higher and cloud tops are typically lower, when more smoke is present. An exception is the morning (6-12 LST), when cloud tops are slightly higher instead under more smoky condition (Fig. 4a), briefly supporting relatively high liquid water paths (Fig. 4b) and encouraging drizzles (Fig. 4c). This is reminiscent of the morning cumulus invigoration documented for August (see Fig. 8b in ZZ19) when more smoke is present in the BL. Rain frequency is reduced throughout the day (Fig.
185   4c), most pronounced in the afternoon where cloud LWP is also substantially reduced (Fig. 4b), compared to a less smoky BL. The low-cloud fraction is reduced over a larger area than just at Ascension when the boundary layer is smokier (Fig. 4d).

When more smoke is present, the entire boundary layer is warmer by ∼0.3 K (Fig. 4e). The boundary layers are more decoupled, with a more moist sub-cloud layer and a drier cloud layer (Fig. 4e), consistent with the reduction in cloudiness. Given that smokier conditions last for a few days (Fig. 2a), the shortwave absorbing can continue to warm the sub-cloud layer
190   over multiple days, extending through the night (shown for August in ZZ19), producing a boundary-layer semi-direct effect.

An aerosol-cloud microphysical interaction is also apparent in the doubling of the satellite-derived N_d (see values printed on Fig. 4e left panel). The radiosonde-derived wind speeds indicate slightly weaker free tropospheric winds when the boundary layer is more smoky, but ERA5-derived atmospheric circulation patterns are not significantly different (not shown). The lack of strong synoptic variations suggests the observed low-cloud variability is driven more strongly by the presence of the shortwave-

195 absorbing smoke in the boundary layer.

5 September: mid-latitude disturbances raise boundary layer heights on cleaner days

Previous studies assessing the impact of above-cloud absorbing aerosol on the boundary layer height are not in full agreement. The regional modeling studies of Sakaeda et al. (2011) and Lu et al. (2018) report an increase in cloud-top heights when biomass burning aerosols are present above clouds, attributed to a reduced free-tropospheric subsidence caused by aerosol heating.

200 Lu et al. (2018) further show an enhanced cloud-top entrainment, when the smoke layer is in contact with the cloud layer, increasing N_d, can account for half of the cloud-top height increase. In contrast, observational studies report a reduction in the cloud top height (e.g., Wilcox, 2010, 2012; Adebiyi et al., 2015) which could be explained by an enhanced lower-tropospheric stability that reduces cloud-top entrainment, as shown within higher-resolution process modeling studies (Johnson et al., 2004; Herbert et al., 2020; Yamaguchi et al., 2015; Zhou et al., 2017) less able to resolve a feedback on the free-tropospheric model

205 velocity. A recent climate-scale modeling study (Gordon et al., 2018) also produces a decrease in boundary layer depth under a plume of biomass burning smoke, when the model free-tropospheric conditions are nudged to reanalysis. The change in boundary layer height accompanying free-tropospheric aerosol is important to clarify, because more shallow boundary layer heights tend to be better coupled to the surface (Zuidema et al., 2009), with the surface moisture fluxes better able to sustain higher cloud fractions.

210 The radar-derived cloud vertical structure at Ascension independently indicates persistent cloud top heights throughout the day in September, regardless of the overhead smoke loading (Fig. 5a). The radar-derived cloud top height varies little with smoke loading, with a slight increase after sunset on days with more smoke. More clear is that cloud frequencies at all levels, more pronouncedly in the lower levels, are higher, by at most ∼20%, when more smoke is present (Fig. 5a). Surface observers do not report a clear shift in low cloud type as a function of smoke loading (Fig. 3b). The radiosonde profiles do

215 differ significantly between the two composites, and a focus on the cleaner conditions provides an alternative perspective from one focused on the smokier conditions. When the free troposphere is less aerosol-laden, the boundary layer is less humid (q_v, RH decrease of 1 g kg^{-1}, ∼5%), cooler within the cloud layer (∼1K at inversion base), with a better-defined inversion base (Fig. 5b). The changes in the free troposphere are equally dramatic: much weaker winds, less moisture, and more stable thermodynamic structure. Differences between the composite-mean N_ds and rBC mass concentrations are statistically

220 insignificant (numbers printed on Fig. 5b), indicating negligible aerosol-cloud microphysical interactions (as expected).

The atmospheric circulations reigning at 700 hPa (Fig. 5c and d) differ significantly between days with low and high free-tropospheric smoke loadings at Ascension. Also expected, on days with more smoke, the AEJ-S extends further westward, and backtrajectories from Ascension near cloud top clearly trace back to continental Africa (Fig. 5c). On days will little smoke,

the main circulation at 700 hPa is anticyclonic about a deeper land-based pressure high, constraining the aerosol closer to the
coast and further south, and away from Ascension. Instead, the above-cloud air is more likely to come from the north and
west of Ascension on these days (Fig. 5d). A primary distinction between the two composite circulations is a disruption of the
mid-latitude eastward flow, with a high-pressure ridge at 700 hPa counteracting the free-tropospheric zonal jet.

Counterintuitively, subsidence above cloud top is stronger, on the less-smoky days when boundary layer at Ascension is
not lower (Fig. 5a, b , e and g), and only weaker at pressures < 650 hPa (Fig. 5g). This shift in subsidence also reflects the
mid-latitude intrusion: an anomalous convergence, reflected in anomalous westerlies weakening the free-tropospheric winds,
supports an anomalous subsidence (Fig. 5e) that is most pronounced to the east of the 700 hPa pressure ridge (right above the
region bounded by Ascension and St. Helena), where the flow shifts from cyclonic to anti-cyclonic and the AEJ-S receives
the strongest weakening (Fig. 5d). At the surface, the mid-latitude disturbance strengthens the south Atlantic high and shifts
it slightly to the southwest (not shown), strengthening the southerlies in the boundary layer, although weakly felt over As-
cension region (Fig. 5g, cyan vectors). Closer to St. Helena, the prevailing southeasterly boundary layer flow is weaken by
the anomalous westerlies, corresponding to the upper-level (700 hPa) mid-latitude disturbance. These changes in the regional
atmospheric circulation is correlating with a pronounced cloudiness reduction of the main southeast Atlantic stratocumulus
deck, except at the northern edge of the deck (including at Ascension), on days when the mid-latitude intrusion is present (Fig.
5f).

St. Helena Island is located approximately 2 days upwind within the boundary layer flow, with Lagrangian forward trajec-
tories from St. Helena placing boundary layer air near if slightly west of Ascension (Fig. 7 within Zuidema et al., 2015). A
height cross-section between Ascension Island and St. Helena Island (16° S, 6° W; gray dashed line on Fig. 5e), indicates a
consistent structure to the free-tropospheric subsidence change between days with low/high free-tropospheric smoke loadings
(Fig. 5g). As such, the radiosondes at St. Helena provide insight into the 24-48 hour cloud adjustment time scale to large-scale
environmental conditions (Klein et al., 1995; Mauger and Norris, 2010; Eastman et al., 2016), with a 2 day lead incorporated
into the St. Helena comparisons between low/high smoke days in Figure 6.

The boundary layer heights are pronouncedly higher at St. Helena, with a much weaker gradient in temperature and moisture
across the cloud top inversion, on the days with less smoke (Fig. 6a), indicating that part of the reason that cloud tops at
Ascension are not lower given stronger subsidence is simply advection of an deeper boundary layer upstream. The potential
temperature, q_v and relative humidity vertical structure differences are qualitatively similar to those at Ascension (Fig. 6a).
The boundary layer is deeper and less humid near the surface (Fig. 6a), and the lower-tropospheric stability is substantially
reduced, on days with less smoke overhead. The boundary layer southerlies extend up to 2 km (Fig. 6a) before reversing in
response to the deeper land-based heat low. Spatial climatologies indicate the radiosonde composites are representing a larger
pattern (Figs. 6b-e). Important for the boundary layer cloud characteristics, the strengthened surface Atlantic high encourages
advection of air off the Southern Ocean by near-surface winds (Fig. 6d, black contours and gray vectors). A pronounced
decrease in lower-tropospheric stability near and south of St. Helena (Fig. 6d, colored contours) is in full agreement with
the radiosonde profiles sampled over St. Helena (Fig. 6a) for low smoke loading days. This can be explained by anomalous
negative horizontal temperature advections at 800 hPa (Fig. 6e, colored contours), as a result of anomalous southerly flows

(gray vectors) corresponding to negative geopotential height anomalies at 800 hPa (black contours). The MODIS-derived low-
260   level cloudiness is substantially reduced and disrupted west of the prime meridian (Fig. 6c, colored contours), compared to
days dominated by free-tropospheric flow off of the continent.(Fig. 6b).

These mid-latitude disturbances, also discussed within Baró Pérez et al. (2020), were most frequent in September of 2016-
2017 and appear consistent with the climatology of Fuchs et al. (2017). Other examples are documented in Diamond et al.
(2018); Adebiyi and Zuidema (2018); Abel et al. (2020). A longer-term analysis might be needed to verify if September
265   captures the climatological annual mean of such intrusions. September does represent a transition month when the continent
is warming up but the ocean is still cool and the mid-latitude westerlies are positioned further north, similar to the southeast
Pacific (Painemal et al., 2010). Pennypacker et al. (2020) document that ultra-clean days at Ascension are most common during
September, although only attribute these partially to a Southern Ocean origin.

6   Increased cloud cover in October

270   Later in the season, during September and October, the temperature gradient between the continental heat low in southern
Africa and equatorial convection encourages a maximum in free-tropospheric easterlies (Tyson et al., 1996; Nicholson and
Grist, 2003; Adebiyi and Zuidema, 2016), that is largely responsible for the westward long-range transport of the biomass
burning smoke within a deep continental boundary layer reaching up to 5-6 km. This encourages smoke to predominantly stay
in the free-troposphere over the southeast Atlantic (Fig. 1 and 2a). The radar-derived cloud vertical structure during October
275   2016 does not appear to vary significantly with the free-tropospheric smoke loading (Fig. 7a). There is some indication that the
cloud layer rises under smokier conditions, with higher cloud bases consistent with a reduced sub-cloud relative humidity (Fig.
7c), and higher cloud tops, particularly in the afternoon. The linear increase in cloud frequency with height indicates much of
the cloud is stratiform, regardless of the smoke loading. Surface observations indicate more stratiform clouds under smokier
conditions (Fig. 3b). Cloud liquid water paths are less and rain is less frequent under smokier conditions (Fig. 7b). Combined,
280   these observations suggest smokier conditions correspond with thinner stratiform cloud layers near the trade-wind inversion.
Figure 7c indicates slightly warmer and drier sub-cloud layers, and otherwise little difference in the potential temperature
profiles of the two composites. The moisture and wind profiles clearly differ, with more moisture overhead between 1.5-3.5km
and stronger winds from the surface to 4km on days with more free-tropospheric smoke. The increase in free-tropospheric
moisture immediately above the cloud tops reduces the relative humidity gradient, and should help sustain the stratiform cloud
285   layer through suppressing evaporative drying by cloud-top entrainment. Fig. 7d indicates a broad, zonally-oriented band of
elevated τ_{af}, also seen in ACAOD (not shown). More interestingly, the satellite-derived low-cloud fraction is enhanced west of
5° W by up to 0.35 (including at Ascension), and slightly reduced to the south, east of 0° E by at most 0.1 (Fig. 7e), indicating
a more zonally-oriented, westward extending cloud deck, when more smoke is present overhead.

In October, an anomalous offshore anti-cyclonic circulation at 700 hPa offshore of continental Africa indicates a strength-
290   ening of the dominating large-scale circulation on the days when the smoke loading is elevated over Ascension (Fig. 7f),
consistent with the measured stronger winds. The free-tropospheric subsidence is reduced underneath the strengthened easter-

lies centered on 10° S, consistent with a secondary circulation (Adebiyi and Zuidema, 2016) and explaining the slight increase in cloud top heights at Ascension on smokier days. Also notable in Fig. 7f is the enhancement in the subsidence just off of the coast of Namibia to the southwest of the strengthened anticyclonic high, correlating with a local increase in N_d on days with

295 more smoke (Fig. 7g). The contrasting decrease in N_d over a narrow region confined within ∼2° along the coast of Namibia on more smoky days (Fig. 7g) correlates with anomalously near-surface northerly flows (gray vectors on Fig. 7g). This circulation pattern advects moist, warm air along the coast of Namibia that encourages inland fog (Andersen et al., 2020). Although beyond the scope of this study, if the increase in moisture increases droplet collision/coalescence, it could limit the number of cloud droplets in the clouds.

300 More significant to the offshore clouds is the broad expanse of increased N_d, stretching from near the Namibian coast to beyond Ascension. At Ascension, the composite-mean MODIS-Meyer derived N_d and surface-based rBC almost double between the high versus low smoke conditions (printed on Fig. 7c). Christensen et al. (2020) select days with enhanced clear-sky τ_a to the south of the main stratocumulus deck, and find an increase in cloud fraction/lifetime far downwind within Lagrangian trajectories, consistent with the increased low-cloud fraction to the west in Fig. 7e. This, along with the rain

305 suppression occurring on smokier days and little change in the lower tropospheric stability (Fig. 7b and c), supports the idea that an aerosol lifetime effect (Albrecht, 1989) is active, consistent with Christensen et al. (2020). To this we can add that the increase in free-tropospheric moisture also helps maintain the cloud against entrainment-driven cloud thinning. The elevated N_d on more smoky days can also contribute to the significant brightening of the cloudy scene near Ascension in October, despite the reduction in cloud liquid water path (all told, a net ∼0.05 increase in TOA all-sky albedo; Fig. 3c). We lack an

310 explanation for the smaller reduction in cloud fraction to the south of the main stratocumulus deck.

7 Longwave cooling by water vapor helps mix the free-troposphere

In September, when more absorbing aerosol is present, the free-troposphere is also more humid and better-mixed over Ascension and St. Helena, compared to the cleaner condition (Fig. 5a and Fig. 6a). Individual profiles often indicate clear colocations between the elevated humid layer and the aerosol layer (see examples in ZZ19 supplement, Adebiyi et al., 2015; Deaconu et al.,

315 2019). The aerosol/humidity layer may have already been well-mixed when leaving the continent of Africa; here we show that longwave cooling at the top of the humidity layers also helps support small-scale mixing. The individual free-tropospheric humidity layers typically include a stability cap at the top, ensuring a sharp gradient to the water vapor mixing ratio, with q_v capable of reducing to near 0 g kg^{-1} above the aerosol layer, reflecting the large-scale subsidence. This provides a strong exposure of the underlying water vapor to outer space, creating a longwave radiative cooling profile that is maximized at

320 the layer-top and helps maintain the stability cap (Mapes and Zuidema, 1996). A negative buoyancy, generated at the top of these layers, can aid downward mixing. Although the longwave cooling from the additional water vapor transported within the aerosol layers is typically small compared to that from the aerosol shortwave absorption (Marquardt Collow et al., 2020), the vertical structure of the radiative heating is also altered, with most of the longwave cooling occurring above the maximum in the shortwave heating from aerosol. It is this displacement that helps maintain a better-mixed aerosol/humidity layer.

325   An example is made of a characteristic profile over Ascension from September 2nd, 2017 with clearly colocated and well-mixed aerosol extinction (derived from the micro-pulse lidar according to Delgadillo et al., 2018) and humidity vertical structures (Fig. 8). Radiative transfer calculations are based on a noon solar zenith angle, a single scattering albedo (at 500 nm) of 0.8 (Zuidema et al., 2018), and an asymmetry parameter of 0.67 loosely based on (Cochrane et al., 2021). These yield a "bench-shaped" longwave cooling profile, maximized at $\sim$-28 K day^{-1}. As expected, the noon-time shortwave heating pro-

330   duced by the smoke is larger, with a maximum of $\sim$34 K day^{-1}. However, the maximum shortwave heating occurs lower in the atmosphere than the maximum longwave cooling. As a result, a net cooling ($\sim$-5 K day^{-1}) pervades the top 100 m of the layer, even during the time of day when the shortwave warming is strongest. The net heating profile encourages small-scale vertical mixing that can allow aerosol to move short distances more freely as well, regardless of time of day. Although such mixing is not deep, based on a simple diabatic heating/static stability calculation, it does help explain why the free-troposphere

335   is typically stratified, as seen in lidar data (Redemann et al., 2021) and individual soundings (see also Pistone et al., 2021).

The free troposphere is better-mixed in September than in October. Although a thorough explanation is beyond the scope of this study, convection over land is more likely to be dry in September than in October (Adebiyi et al., 2015; Redemann et al., 2021), with the warming land surface establishing a continental boundary layer capable of reaching 5 km (Pistone et al., 2021). In contrast, more of the convection in October is moist, reflecting a southward seasonal march of the intertropical convergence

340   zone (Adebiyi et al., 2015). This may not distribute moisture as evenly in the atmosphere initially as does dry convection.

8   Concluding remarks

This study characterizes the sub-seasonal evolution of the marine boundary layer clouds over the remote southeast Atlantic, from July to October during 2016 and 2017, as a function of the aerosol loading and its vertical distribution. This extends Zhang and Zuidema (2019), which focused on August only, and is distinguished from previous studies that apply some form

345   of seasonal averaging (e.g., Wilcox, 2010, 2012; Costantino and Bréon, 2013; Adebiyi and Zuidema, 2018; Deaconu et al., 2019). This is done primarily because of the dramatic rise in altitude of the aerosol mass centroid during July to October over the southeast Atlantic. Smoke episodes arriving at Ascension Island mainly occupy the boundary layer in July, with the boundary layer smoke loading reaching a maximum at Ascension in August. Smoke within the free troposphere also becomes more frequent in September and that within the boundary layer reduces dramatically. In October, the free-tropospheric zonal

350   winds reaching Ascension remain strong but are more likely to transport moisture than aerosol. This overall evolution in synoptic regimes occurs approximately 2 weeks later in 2017 than 2016 (Fig. 1-2). This evolution affects which aerosol-cloud interactions are likely to dominate, but is also clearly linked to meteorological features that may dominate the cloud response. Key findings are:

1. When smoke is present, the seasonal evolution in low cloud amount, in which the low cloud amount increases and

355   becomes more stratiform and less cumuliform from July to October, is amplified. The cloudiness changes dominate the top-of-atmosphere all-sky albedo change associated with the smoke intrusions (Fig. 3).

2. In July, cloud cover, cloud LWP and rain occurrence are reduced when more smoke is present, at all times of day but particularly in the afternoon. The thermodynamic and wind vertical structure is similar between days with more/less smoke, suggesting variability in the smoke loading is driven more by changes in emissions rather than synoptics (Fig. 4). A morning increase in liquid water path, even under smokier conditions, is similar to a recoupling of the cloud layer to the sub-cloud layer detailed more comprehensively for August in ZZ19 in the late morning.

3. A focus on the days with less free-tropospheric smoke over Ascension in September provides a different synoptic perspective to changes in the boundary layer height previously related to the presence of free-tropospheric smoke. Days with less aerosol over Ascension are distinguished by mid-latitude synoptic intrusions into the subtropics. An upper-level pressure ridge constrains the circulation around the land-based heat low to the coastal region, reducing the westward extent of the free-tropospheric zonal winds at $10°$S that normally disperse aerosol (Fig. 5). A strengthened surface anticyclone over the Atlantic strengthens boundary layer southerlies more likely to advect Southern Ocean air. The lower tropospheric stability is reduced, despite stronger synoptically-aided subsidence, helping to raise the boundary layer top, particularly noticeable at St. Helena Island (Fig. 6).

4. In October, the free-tropospheric zonal winds that advect aerosol further offshore are stronger when more aerosol is present over Ascension. This also enhances the humidity above the cloud top, reducing entrainment-driven evaporative drying. This helps support the increased occurrence of stratiform clouds and large-scale enhancement in the satellite-derived low-cloud fraction. Cloud tops are slightly higher at Ascension when the smoke loading is higher, consistent with reduced subsidence associated with the strong zonal winds (Fig. 7). Possible aerosol indirect effect indicated by the doubling of cloud droplet number concentration (N_d) is likely to contribute to prolonging the lifetime and enhancing the brightness (Fig. 3c) of the stratiform clouds. These two effects (an additional moisture source and an aerosol cloud lifetime effect) may help explain why the low-cloud fraction is higher, despite a lower liquid water path, compared to the southeast Pacific stratocumulus deck during this time of year (Zuidema et al., 2016).

5. The sharp gradient in water vapor mixing ratio at the top of a free-tropospheric aerosol layer generates a net cooling at the layer-top, even at solar noon, and is offset vertically from the larger shortwave warming occurring below through aerosol absorption. The negative buoyancy can facilitate a downward vertical mixing that also allows the free-tropospheric aerosol to move vertically more freely (Fig. 8). This effect helps maintain the notably well-mixed September free-tropospheric thermodynamic profiles. These profiles are less well-mixed in October (Fig. 7c), which may reflect the greater prevalence of moist convection over the continent.

Previous studies applying a seasonal averaging successfully isolate a cloud thickening when more aerosol is present in the free troposphere, but have typically overlooked a cloud reduction when more smoke is present in the boundary layer. It may have required recent field campaigns to better appreciate that the boundary layer can also be smoky. The cloudiness changes are most dramatic over the main stratocumulus region in September (Fig. 5f), in part because of a substantial cloud clearing during the less smoky time periods. Fig. 3c also indicates that over the July to October time frame, the all-sky albedo changes

390 in October are the most dramatic near Ascension, in part because higher cloud fractions then and potentially an aerosol-induced cloud brightening effect. Thus, this study also helps raise the point that seasonally averaged changes in the regional radiation budget induced by biomass burning aerosols might be dominated by the signal from October, which then helps explain why the boundary layer semi-direct effect has been difficult to isolate in previous studies over the southeast Atlantic.

Data availability. The LASIC ground-based datasets are publicly available from the ARM Climate Research Facility (https://www.arm.gov/
395 research/campaigns/amf2016lasic). The HYSPLIT model is publicly available from the NOAA Air Resources Laboratory (https://www.arl.
noaa.gov/hysplit/). The UK Met Office SYNOP hourly weather reports are publicly available from the CEDA archive of the Met Office
Integrated Data Archive System (MIDAS, http://catalogue.ceda.ac.uk/uuid/77910bcec71c820d4c92f40d3ed3f249). The RRTMG code is
publicly available from the AER website (http://rtweb.aer.com/). The MODIS Level-3 datasets are publicly available from NASA's Level-3
and Atmosphere Archive & Distribution System Distributed Active Archive Center (https://ladsweb.modaps.eosdis.nasa.gov/). The SEVIRI
400 retrievals and CERES SSF data are publicly available from NASA's Langley Research Center (https://satcorps.larc.nasa.gov/). The fifth-
generation ECMWF (ERA5) atmospheric reanalyses of the global climate data are available through the Copernicus Climate Change Service
(C3S, https://cds.climate.copernicus.eu/). The above-cloud aerosol optical depth (ACAOD) dataset is available upon request.

Author contributions. JZ and PZ conceived this study. JZ analyzed the results, and PZ contributed to their interpretation. JZ wrote the manuscript with edits from PZ.

Competing interests. The authors declare that they have no conflict of interest.

Acknowledgements. This research is supported by the U.S. Department of Energy, Office of Science (grants DE-SC0018272 and DE-SC0021250). We are indebted to the LASIC scientists, instrument mentors, and logistics staff who made this analysis possible through their efforts in deploying and maintaining the instruments, and processing and calibrating the campaign datasets. We thank Kerry Meyer for providing the MODIS-derived above-cloud aerosol optical depth (ACAOD) product.

References

Abel, S. J., Barrett, P. A., Zuidema, P., Zhang, J., Christensen, M., Peers, F., Taylor, J. W., Crawford, I., Bower, K. N., and Flynn, M.: Open cells exhibit weaker entrainment of free-tropospheric biomass burning aerosol into the south-east Atlantic boundary layer, Atmos. Chem. Phys., 20, 4059–4084, https://doi.org/10.5194/acp-20-4059-2020, 2020.

Ackerman, A. S., Toon, O. B., Stevens, D. E., Heymsfield, A. J., Ramanathan, V., and Welton, E. J.: Reduction of tropical cloudiness by soot, Science, 288, 1042 –1047, https://doi.org/doi: 10.1126/science.288.5468.1042, 2000.

Adebiyi, A. A. and Zuidema, P.: The role of the southern African easterly jet in modifying the southeast Atlantic aerosol and cloud environments, Q. J. Roy. Meteor. Soc., 142, 1574–1589, https://doi.org/10.1002/qj.2765, 2016.

Adebiyi, A. A. and Zuidema, P.: Low Cloud Cover Sensitivity to Biomass-Burning Aerosols and Meteorology over the Southeast Atlantic, J. Climate, 31, 4329–4346, https://doi.org/10.1175/JCLI-D-17-0406.1, 2018.

Adebiyi, A. A., Zuidema, P., and Abel, S. J.: The Convolution of Dynamics and Moisture with the Presence of Shortwave Absorbing Aerosols over the Southeast Atlantic, J. Climate, 28, 1997–2024, https://doi.org/10.1175/JCLI-D-14-00352.1, 2015.

Albrecht, B. A.: Aerosols, Cloud Microphysics, and Fractional Cloudiness, Science, 245, 1227–1230, https://doi.org/10.1126/science.245.4923.1227, 1989.

Andersen, H., Cermak, J., Fuchs, J., Knippertz, P., Gaetani, M., Quinting, J., Sippel, S., and Vogt, R.: Synoptic-scale controls of fog and low-cloud variability in the Namib Desert, Atmos. Chem. Phys., 20, 3415–3438, https://doi.org/10.5194/acp-20-3415-2020, 2020.

Baró Pérez, A., Devasthale, A., Bender, F., and Ekman, A. M. L.: Impact of absorbing and non-absorbing aerosols on radiation and low-level clouds over the southeast Atlantic from co-located satellite observations, Atmos. Chem. Phys. Discuss., manuscript, 1–22, https://doi.org/10.5194/acp-2020-1089, 2020.

Che, H., Stier, P., Gordon, H., Watson-Parris, D., and Deaconu, L.: Cloud adjustments dominate the overall negative aerosol radiative effects of biomass burning aerosols in UKESM1 climate model simulations over the south-eastern Atlantic, Atmos. Chem. Phys., 21, https://doi.org/10.5194/acp-21-17-2021, 2021.

Christensen, M. W., Jones, W. K., and Stier, P.: Aerosols enhance cloud lifetime and brightness along the stratus-to-cumulus transition, P. Natl. Acad. Sci. USA, 117, 17 591–17 598, https://doi.org/10.1073/pnas.1921231117, 2020.

Clough, S. A., Shephard, M. W., Mlawer, E. J., Delamere, J. S., Iacono, M. J., Cady-Pereira, K., Boukabara, S., and Brown, P. D.: Atmospheric radiative transfer modeling: A summary of the AER codes, Journal of Quantitative Spectroscopy & Radiative Transfer, 91, 233–244, https://doi.org/10.1016/j.jqsrt.2004.05.058, 2005.

Cochrane, S. P., Schmidt, K. S., Chen, H., Pilewskie, P., Kittelman, S., Redemann, J., LeBlanc, S., Pistone, K., Kacenelenbogen, M., Segal Rozenhaimer, M., Shinozuka, Y., Flynn, C., Dobracki, A., Zuidema, P., Howell, S., Freitag, S., and Doherty, S.: Empirically-Derived Parameterizations of the Direct Aerosol Radiative Effect based on ORACLES Aircraft Observations, Atmos. Meas. Tech., 14, 567–593, https://doi.org/10.5194/amt-14-567-2021, 2021.

Costantino, L. and Bréon, F.-M.: Aerosol indirect effect on warm clouds over South-East Atlantic, from co-located MODIS and CALIPSO observations, Atmos. Chem. Phys., 13, 69 – 88, https://doi.org/10.5194/acp-13-69-2013, 2013.

Deaconu, L. T., Ferlay, N., Waquet, F., Peers, F., Thieuleux, F., and Goloub, P.: Satellite inference of water vapour and above-cloud aerosol combined effect on radiative budget and cloud-top processes in the southeastern Atlantic Ocean, Atmos. Chem. Phys., 19, 11 613–11 634, https://doi.org/10.5194/acp-19-11613-2019, 2019.

Delgadillo, R., Voss, K. J., and Zuidema, P.: Characteristics of Optically Thin Coastal Florida Cumuli Derived From Surface-Based Lidar Measurements, J. Geophys. Res.-Atmos., 123, 10,591–10,605, https://doi.org/10.1029/2018JD028867, 2018.

Diamond, M. S., Dobracki, A., Freitag, S., Small Griswold, J. D., Heikkila, A., Howell, S. G., Kacarab, M. E., Podolske, J. R., Saide, P. E., and Wood, R.: Time-dependent entrainment of smoke presents an observational challenge for assessing aerosol–cloud interactions over

450   the southeast Atlantic Ocean, Atmos. Chem. Phys., 18, 14 623–14 636, https://doi.org/10.5194/acp-18-14623-2018, 2018.

Draxler, R. R. and Hess, G. D.: An Overview of the HYSPLIT 4 Modelling System for Trajectories, Dispersion, and Deposition, Aust. Meteorol. Mag., 47, 295 –308, 1998.

Eastman, R., Wood, R., and Bretherton, C. S.: Time Scales of Clouds and Cloud-Controlling Variables in Subtropical Stratocumulus from a Lagrangian Perspective, J. Atmos. Sci, 73, 3079–3091, https://doi.org/10.1175/JAS-D-16-0050.1, 2016.

455   Fuchs, J., Cermak, J., Andersen, H., Hollmann, R., and Schwarz, K.: On the Influence of Air Mass Origin on Low-Cloud Properties in the Southeast Atlantic, J. Geophys. Res.-Atmos., 122, 11 076–11 091, https://doi.org/https://doi.org/10.1002/2017JD027184, 2017.

Gordon, H., Field, P. R., Abel, S. J., Dalvi, M., Grosvenor, D. P., Hill, A. A., Johnson, B. T., Miltenberger, A. K., Yoshioka, M., and Carslaw, K. S.: Large simulated radiative effects of smoke in the south-east Atlantic, Atmos. Chem. Phys., 18, 15 261–15 289, https://doi.org/10.5194/acp-18-15261-2018, 2018.

460   Haywood, J. M., Abel, S. J., Barrett, P. A., Bellouin, N., Blyth, A., Bower, K. N., Brooks, M., Carslaw, K., Che, H., Coe, H., Cotterell, M. I., Crawford, I., Cui, Z., Davies, N., Dingley, B., Field, P., Formenti, P., Gordon, H., de Graaf, M., Herbert, R., Johnson, B., Jones, A. C., Langridge, J. M., Malavelle, F., Partridge, D. G., Peers, F., Redemann, J., Stier, P., Szpek, K., Taylor, J. W., Watson-Parris, D., Wood, R., Wu, H., and Zuidema, P.: Overview: The CLoud-Aerosol-Radiation Interaction and Forcing: Year-2017 (CLARIFY-2017) measurement campaign, Atmos. Chem. Phys., 21, 1049–1084, https://doi.org/10.5194/acp-21-1049-2021, 2021.

465   Herbert, R. J., Bellouin, N., Highwood, E. J., and Hill, A. A.: Diurnal cycle of the semi-direct effect from a persistent absorbing aerosol layer over marine stratocumulus in large-eddy simulations, Atmos. Chem. Phys., 20, 1317–1340, https://doi.org/10.5194/acp-20-1317-2020, 2020.

Hersbach, H., Bell, B., Berrisford, P., Hirahara, S., Horányi, A., Muñoz-Sabater, J., Nicolas, J., Peubey, C., Radu, R., Schepers, D., Simmons, A., Soci, C., Abdalla, S., Abellan, X., Balsamo, G., Bechtold, P., Biavati, G., Bidlot, J., Bonavita, M., De Chiara, G., Dahlgren, P., Dee,

470   D., Diamantakis, M., Dragani, R., Flemming, J., Forbes, R., Fuentes, M., Geer, A., Haimberger, L., Healy, S., Hogan, R. J., Hólm, E., Janisková, M., Keeley, S., Laloyaux, P., Lopez, P., Lupu, C., Radnoti, G., de Rosnay, P., Rozum, I., Vamborg, F., Villaume, S., and Thépaut, J.-N.: The ERA5 global reanalysis, Q. J. Roy. Meteor. Soc., 146, 1999–2049, https://doi.org/10.1002/qj.3803, 2020.

Johnson, B. T.: Large-eddy simulations of the semidirect aerosol effect in shallow cumulus regimes, J. Geophys. Res.-Atmos., 110, D14 206, https://doi.org/10.1029/2004JD005601, 2005.

475   Johnson, B. T., Shine, K. P., and Forster, P. M.: The semi-direct aerosol effect: Impact of absorbing aerosols on marine stratocumulus, Q. J. Roy. Meteor. Soc., 130, 1407–1422, https://doi.org/10.1256/qj.03.61, 2004.

Kacarab, M., Thornhill, K. L., Dobracki, A., Howell, S. G., O'Brien, J. R., Freitag, S., Poellot, M. R., Wood, R., Zuidema, P., Redemann, J., and Nenes, A.: Biomass burning aerosol as a modulator of the droplet number in the southeast Atlantic region, Atmos. Chem. Phys., 20, 3029–3040, https://doi.org/10.5194/acp-20-3029-2020, 2020.

480   Klein, S. A. and Hartmann, D. L.: The Seasonal Cycle of Low Stratiform Clouds, J. Climate, 6, 1587–1606, https://doi.org/10.1175/1520-0442(1993)006<1587:TSCOLS>2.0.CO;2, 1993.

Klein, S. A., Hartmann, D. L., and Norris, J. R.: On the Relationships among Low-Cloud Structure, Sea Surface Tempera-
ture, and Atmospheric Circulation in the Summertime Northeast Pacific, J. Climate, 8, 1140–1155, https://doi.org/10.1175/1520-
0442(1995)008<1140:OTRALC>2.0.CO;2, 1995.

485 Levy, R. C., Mattoo, S., Munchak, L. A., Remer, L. A., Sayer, A. M., Patadia, F., and Hsu, N. C.: The Collection 6 MODIS aerosol products
over land and ocean, Atmos. Meas. Tech., 6, 2989–3034, https://doi.org/10.5194/amt-6-2989-2013, 2013.

Lu, Z., Liu, X., Zhang, Z., Zhao, C., Meyer, K., Rajapakshe, C., Wu, C., Yang, Z., and Penner, J. E.: Biomass smoke from southern Africa
can significantly enhance the brightness of stratocumulus over the southeastern Atlantic Ocean, P. Natl. Acad. Sci. USA, 115, 2924–2929,
https://doi.org/10.1073/pnas.1713703115, 2018.

490 Mallet, M., Solmon, F., Nabat, P., Elguindi, N., Waquet, F., Bouniol, D., Sayer, A. M., Meyer, K., Roehrig, R., Michou, M., Zuidema, P.,
Flamant, C., Redemann, J., and Formenti, P.: Direct and semi-direct radiative forcing of biomass burning aerosols over the Southeast
Atlantic (SEA) and its sensitivity to absorbing properties: A regional climate modeling study, Atmos. Chem. Phys., 20, 13 191–13 216,
https://doi.org/10.5194/acp-20-13191-2020, 2020.

Mapes, B. E. and Zuidema, P.: Radiative-Dynamical Consequences of Dry Tongues in the Tropical Troposphere, J. Atmos. Sci, 53, 620–638,
495 https://doi.org/10.1175/1520-0469(1996)053<0620:RDCODT>2.0.CO;2, 1996.

Marquardt Collow, A. B., Miller, M. A., Trabachino, L. C., Jensen, M. P., and Wang, M.: Radiative heating rate profiles over the southeast
Atlantic Ocean during the 2016 and 2017 biomass burning seasons, Atmos. Chem. Phys., 20, 10 073–10 090, https://doi.org/10.5194/acp-
20-10073-2020, 2020.

Mauger, G. S. and Norris, J. R.: Assessing the Impact of Meteorological History on Subtropical Cloud Fraction, J. Climate, 23, 2926–2940,
500 https://doi.org/10.1175/2010JCLI3272.1, 2010.

Meyer, K., Platnick, S., and Zhang, Z.: Simultaneously inferring above-cloud absorbing aerosol optical thickness and under-
lying liquid phase cloud optical and microphysical properties using MODIS, J. Geophys. Res.-Atmos., 120, 5524–5547,
https://doi.org/10.1002/2015JD023128, 2015.

Miller, M. A., Nitschke, K., Ackerman, T. P., Ferrell, W. R., Hickmon, N., and Ivey, M.: The ARM Mobile Facilities, Meteor. Mon., 57,
505 9.1–9.15, https://doi.org/10.1175/AMSMONOGRAPHS-D-15-0051.1, 2016.

Minnis, P., Nguyen, L., Palikonda, R., Heck, P. W., Spangenberg, D. A., Doelling, D. R., Kirk Ayers, J., Smith, W. L., Khaiyer, M. M.,
Trepte, Q. Z., Avey, L. A., Chang, F.-L., Yost, C. R., Chee, T. L., and Szedung, T. L.: Near-real time cloud retrievals from op-
erational and research meteorological satellites, Proc. SPIE 7107, Remote Sensing of Clouds and the Atmosphere XIII, 710 703,
https://doi.org/10.1117/12.800344, 2008.

510 Nicholson, S. E. and Grist, J. P.: The seasonal evolution of the atmospheric circulation over west Africa and equatorial Africa, J. Climate, 16,
1013–1030, https://doi.org/10.1175/1520-0442(2003)016<1013:TSEOTA>2.0.CO;2, 2003.

Painemal, D. and Zuidema, P.: Assessment of MODIS cloud effective radius and optical thickness retrievals over the southeast Pacific with
VOCALS-REx in situ measurements, J. Geophys. Res.-Atmos., 116, 1–16, https://doi.org/10.1029/2011JD016155, 2011.

Painemal, D., Garreaud, R., Rutllant, J., and Zuidema, P.: Southeast Pacific Stratocumulus: High-Frequency Variability and Mesoscale
515 Structures over San Félix Island, J. Appl. Meteorol. Climatol., 49, 463–477, https://doi.org/10.1175/2009JAMC2230.1, 2010.

Pennypacker, S., Diamond, M., and Wood, R.: Ultra-clean and smoky marine boundary layers frequently occur in the same season over the
southeast Atlantic, Atmos. Chem. Phys., 20, 2341–2351, https://doi.org/10.5194/acp-20-2341-2020, 2020.

Pistone, K., Zuidema, P., Wood, R., Diamond, M., da Silva, A. M., Ferrada, G., Saide, P., Ueyama, R., Ryoo, J.-M., Pfister, L., Podolske,
J., Noone, D., Bennett, R., Stith, E., Carmichael, G., Redemann, J., Flynn, C., LeBlanc, S., Segal-Rozenhaimer, M., and Shinozuka, Y.:

520   Exploring the elevated water vapor signal associated with the free-tropospheric biomass burning plume over the southeast Atlantic Ocean, Atmos. Chem. Phys. Discuss., manuscript, 1–39, https://doi.org/10.5194/acp-2020-1322, 2021.

Platnick, S., King, M. D., Ackerman, S. A., Menzel, W. P., Baum, B. A., Riedi, J. C., and Frey, R. A.: The MODIS cloud products: algorithms and examples from Terra, IEEE Trans. Geos. Remote Sens., 41, 459–473, https://doi.org/10.1109/TGRS.2002.808301, 2003.

Redemann, J., Wood, R., Zuidema, P., Doherty, S. J., Luna, B., LeBlanc, S. E., Diamond, M. S., Shinozuka, Y., Chang, I. Y., Ueyama, R.,
525   Pfister, L., Ryoo, J., Dobracki, A. N., da Silva, A. M., Longo, K. M., Kacenelenbogen, M. S., Flynn, C. J., Pistone, K., Knox, N. M., Piketh, S. J., Haywood, J. M., Formenti, P., Mallet, M., Stier, P., Ackerman, A. S., Bauer, S. E., Fridlind, A. M., Carmichael, G. R., Saide, P. E., Ferrada, G. A., Howell, S. G., Freitag, S., Cairns, B., Holben, B. N., Knobelspiesse, K. D., Tanelli, S., L'Ecuyer, T. S., Dzambo, A. M., Sy, O. O., McFarquhar, G. M., Poellot, M. R., Gupta, S., O'Brien, J. R., Nenes, A., Kacarab, M. E., Wong, J. P. S., Small-Griswold, J. D., Thornhill, K. L., Noone, D., Podolske, J. R., Schmidt, K. S., Pilewskie, P., Chen, H., Cochrane, S. P., Sedlacek,
530   A. J., Lang, T. J., Stith, E., Segal-Rozenhaimer, M., Ferrare, R. A., Burton, S. P., Hostetler, C. A., Diner, D. J., Platnick, S. E., Myers, J. S., Meyer, K. G., Spangenberg, D. A., Maring, H., and Gao, L.: An overview of the ORACLES (ObseRvations of Aerosols above CLouds and their intEractionS) project: Aerosol-cloud-radiation interactions in the southeast Atlantic basin, Atmos. Chem. Phys., 21, 1507–1563, https://doi.org/10.5194/acp-21-1507-2021, 2021.

Sakaeda, N., Wood, R., and Rasch, P. J.: Direct and semidirect aerosol effects of southern African biomass burning aerosol, J. Geophys.
535   Res.-Atmos., 116, 1–19, https://doi.org/10.1029/2010JD015540, 2011.

Scott, R. C., Myers, T. A., Norris, J. R., Zelinka, M. D., Klein, S. A., Sun, M., and Doelling, D. R.: Observed Sensitivity of Low-Cloud Radiative Effects to Meteorological Perturbations over the Global Oceans, J. Climate, 33, 7717–7734, https://doi.org/10.1175/JCLI-D-19-1028.1, 2020.

Shinozuka, Y., Saide, P. E., Ferrada, G. A., Burton, S. P., Ferrare, R., Doherty, S. J., Gordon, H., Longo, K., Mallet, M., Feng, Y., Wang, Q.,
540   Cheng, Y., Dobracki, A., Freitag, S., Howell, S. G., LeBlanc, S., Flynn, C., Segal-Rosenhaimer, M., Pistone, K., Podolske, J. R., Stith, E. J., Bennett, J. R., Carmichael, G. R., da Silva, A., Govindaraju, R., Leung, R., Zhang, Y., Pfister, L., Ryoo, J.-M., Redemann, J., Wood, R., and Zuidema, P.: Modeling the smoky troposphere of the southeast Atlantic: A comparison to ORACLES airborne observations from September of 2016, Atmos. Chem. Phys., 20, 11 491–11 526, https://doi.org/10.5194/acp-20-11491-2020, 2020.

Su, W., Corbett, J., Eitzen, Z., and Liang, L.: Next-generation angular distribution models for top-of-atmosphere radiative flux calculation
545   from CERES instruments: methodology, Atmos. Meas. Tech., 8, 611–632, https://doi.org/10.5194/amt-8-611-2015, 2015.

Tyson, P. D., Garstang, M., and Swap, R.: Large-Scale Recirculation of Air over Southern Africa, J. Appl. Meteorol., 35, 2218–2236, https://doi.org/10.1175/1520-0450(1996)035<2218:LSROAO>2.0.CO;2, 1996.

Wielicki, B. A., Barkstrom, B. R., Harrison, E. F., Lee, R. B., Smith, G. L., and Cooper, J. E.: Clouds and the Earth's Radiant Energy System (CERES): An Earth Observing System Experiment, B. Am. Meteor. Soc., 77, 853–868, https://doi.org/10.1175/1520-
550   0477(1996)077<0853:CATERE>2.0.CO;2, 1996.

Wilcox, E. M.: Stratocumulus cloud thickening beneath layers of absorbing smoke aerosol, Atmos. Chem. Phys., 10, 11 769 – 11 777, 2010.

Wilcox, E. M.: Direct and semi-direct radiative forcing of smoke aerosols over clouds, Atmos. Chem. Phys., 12, 139–149, https://doi.org/10.5194/acp-12-139-2012, 2012.

WMO: Manual on Codes, 306, World Meteorological Organization Publications, 1 edn., 1974.

555   Yamaguchi, T., Feingold, G., Kazil, J., and McComiskey, A.: Stratocumulus to cumulus transition in the presence of elevated smoke layers, Geophys. Res. Lett., 42, 10 478–10 485, https://doi.org/https://doi.org/10.1002/2015GL066544, 2015.

Zhang, J. and Zuidema, P.: The diurnal cycle of the smoky marine boundary layer observed during August in the remote southeast Atlantic, Atmos. Chem. Phys., 19, 14 493–14 516, https://doi.org/10.5194/acp-19-14493-2019, 2019.

Zhou, X., Ackerman, A. S., Fridlind, A. M., Wood, R., and Kollias, P.: Impacts of solar-absorbing aerosol layers on the transition of stra-
560   tocumulus to trade cumulus clouds, Atmos. Chem. Phys., 17, 12 725–12 742, https://doi.org/10.5194/acp-17-12725-2017, 2017.

Zuidema, P., Painemal, D., deSzoeke, S., and Fairall, C.: Stratocumulus cloud top height estimates and their climatic implications, J. Climate, 22, 4652–4666, https://doi.org/10.1175/2009JCLI2708.1, 2009.

Zuidema, P., Chiu, C., Fairall, C., Ghan, S., Kollias, P., McFarguhar, G., Mechem, D., Romps, D., Wong, H., Yuter, S., Alvarado, M., DeSzoeke, S., Feingold, G., Haywood, J., Lewis, E., McComiskey, A., Redemann, J., Turner, D., Wood, R., and Zhu, P.: Layered Atlantic
565   Smoke Interactions with Clouds (LASIC) science plan: DOE Office of Science Atmospheric Radiation Measurement (ARM) Program, http://www.osti.gov/scitech/servlets/purl/1232658, 2015.

Zuidema, P., Chang, P., Medeiros, B., Kirtman, B. P., Mechoso, R., Schneider, E. K., Toniazzo, T., Richter, I., Small, R. J., Bellomo, K., Brandt, P., de Szoeke, S., Farrar, J. T., Jung, E., Kato, S., Li, M., Patricola, C., Wang, Z., Wood, R., and Xu, Z.: Challenges and Prospects for Reducing Coupled Climate Model SST Biases in the Eastern Tropical Atlantic and Pacific Oceans: The U.S. CLIVAR Eastern Tropical
570   Oceans Synthesis Working Group, B. Am. Meteor. Soc., 97, 2305–2328, https://doi.org/10.1175/BAMS-D-15-00274.1, 2016.

Zuidema, P., Sedlacek, A. J., Flynn, C., Springston, S., Delgadillo, R., Zhang, J., Aiken, A. C., Koontz, A., and Muradyan, P.: The Ascension Island Boundary Layer in the Remote Southeast Atlantic is Often Smoky, Geophys. Res. Lett., 45, 4456–4465, https://doi.org/10.1002/2017GL076926, 2018.
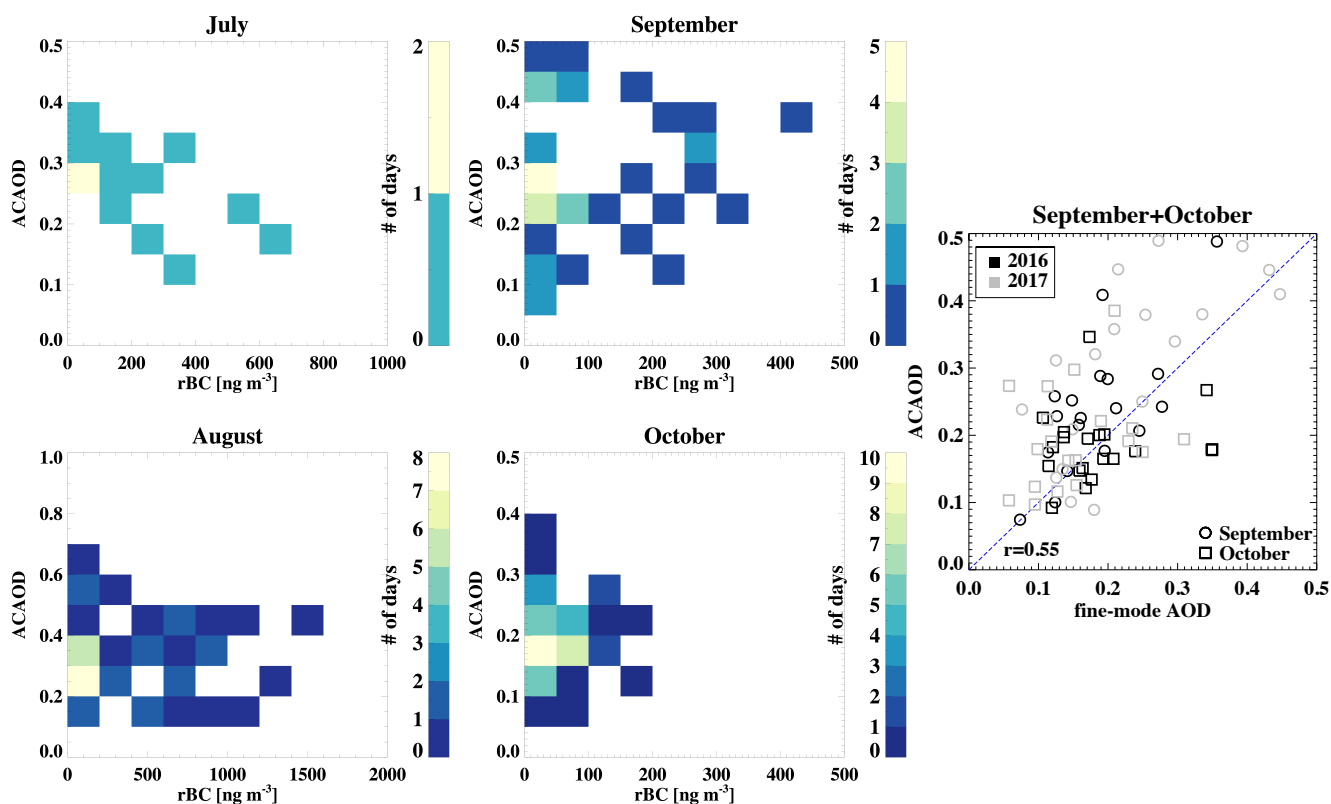
Figure 1. Joint histogram of the MODIS-Meyer above-cloud aerosol optical depth (ACAOD; Meyer et al., 2015) and near-surface rBC mass concentrations for July through October, by month, 2016 and 2017 combined. Note variation on the x- and y-axis ranges and # of contributing days for each month. ACAOD against MODIS-retrieved fine-mode AOD is shown on the right, for September and October. Satellite retrievals shown are 3° by 3° domain-averages.
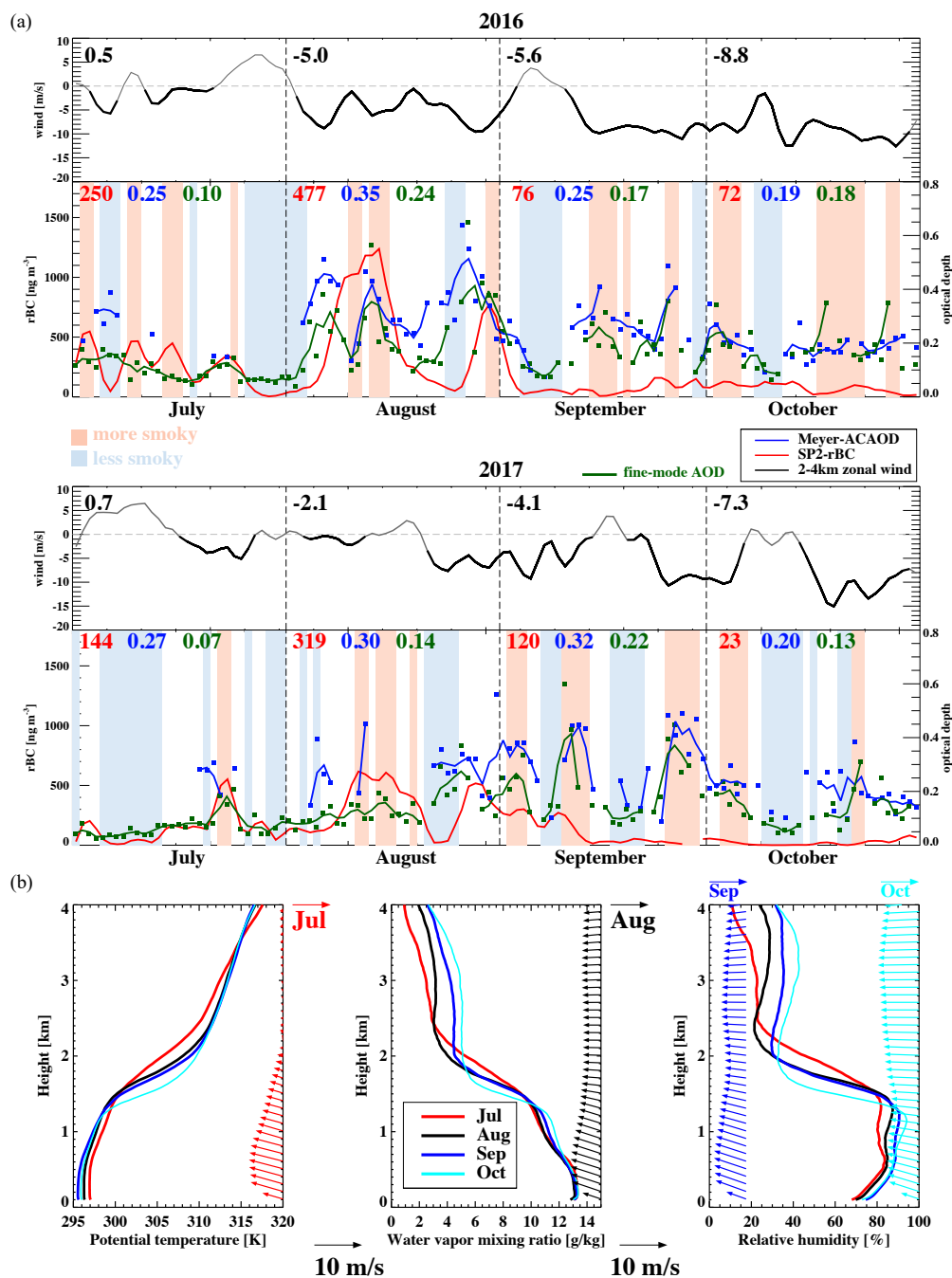
Figure 2. (a) Time-series of daily rBC mass concentrations (red), τ_{AC} (blue), τ_{af} (dark green), and 2-4 km mean zonal winds (gray/black) from July through October for 2016 (upper) and 2017 (bottom). A 3-day running mean is applied to all, easterlies lasting at least 5 days are highlighted with a thicker black line, and monthly mean values are indicated. More/less smoky composites are indicated by light-red/light-blue shadings in the background. **(b)** Monthly-mean radiosonde profiles (0-4 km above sea level) of potential temperature, water vapor mixing ratio, relative humidity, and winds, by month, for 2016 and 2017.
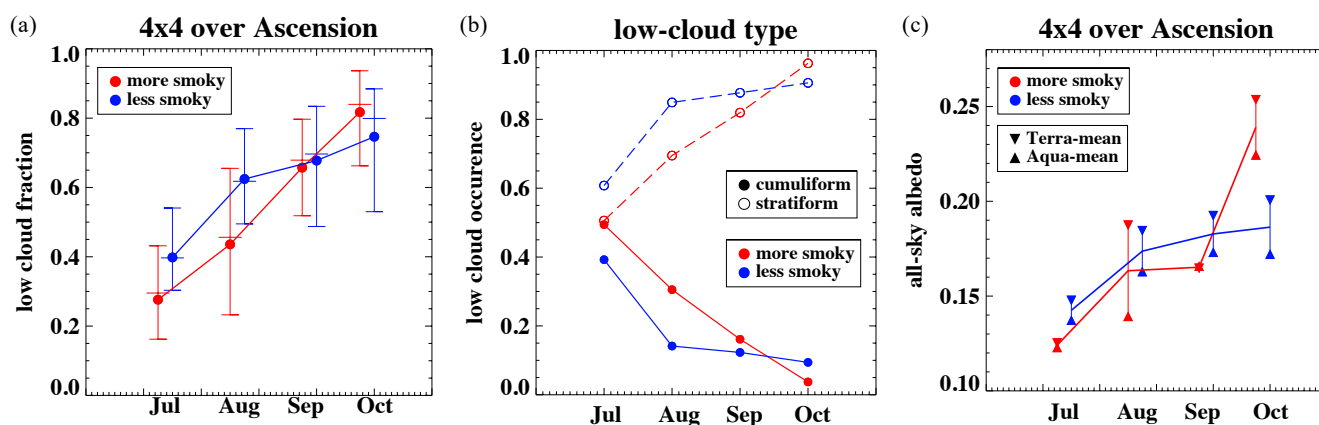
Figure 3. (a) SEVIRI-derived areal-mean ($4°x4°$) low-cloud fraction, with diurnal range and median values also indicated, **(b)** surface-observed cloud type frequency of occurrence (stratiform and cumuliform; empty and filled circles, respectively), and **(c)** all-sky areal-mean CERES albedo, all composited by high and low smoke (red and blue) loadings, including the Terra-only and Aqua-only mean values, as a function of month (July-October).
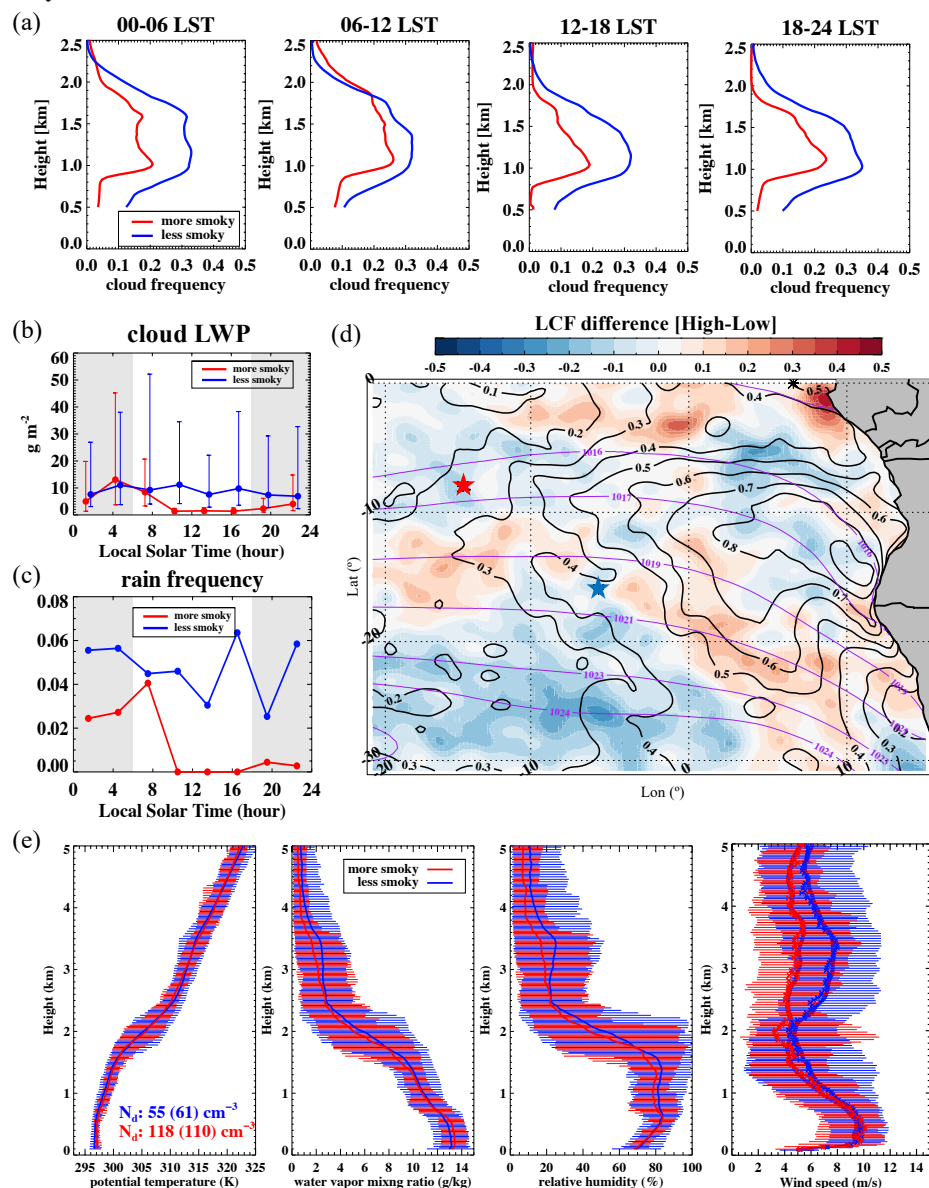
Figure 4. July **(a)** diurnal cycle in the mean cloud frequencies derived using Ka-band zenith pointing cloud radar (KAZR) reflectivities > -35 dBZ at their vertical resolution of 30 m. **(b)** Diurnal cycle of cloud liquid water paths at the airport for July 2017, shown as medians (filled circles) and interquartile ranges (vertical bars). **(c)** Disdrometer-derived rain frequencies, at the AMF1 site, shown as 3-hour aggregations of one-minute samples with rain rates exceeding 0 mm/hr. **(d)** Difference in MODIS daily liquid cloud fraction (LCF; filled-contours, high smoke minus low smoke), overlaid with July-mean sea level pressure (hPa, purple) and LCF (black). Ascension Island and St. Helena Island locations indicated with red and blue stars respectively. **(e)** Radiosonde profiles (0-5 km above sea level) of potential temperature (θ), water vapor mixing ratio (q_v), relative humidity (RH), and wind speed, horizontal bars indicate 10th and 90th percentile values. Composite-mean (-median) of MODIS-Meyer N_d ($2°$ by $2°$ over Ascension) is indicated on the first panel. **(a)-(c)** and **(e)** are composited by high smoke (red) and low smoke (blue) conditions. 2016 and 2017 data are combined unless specified otherwise.
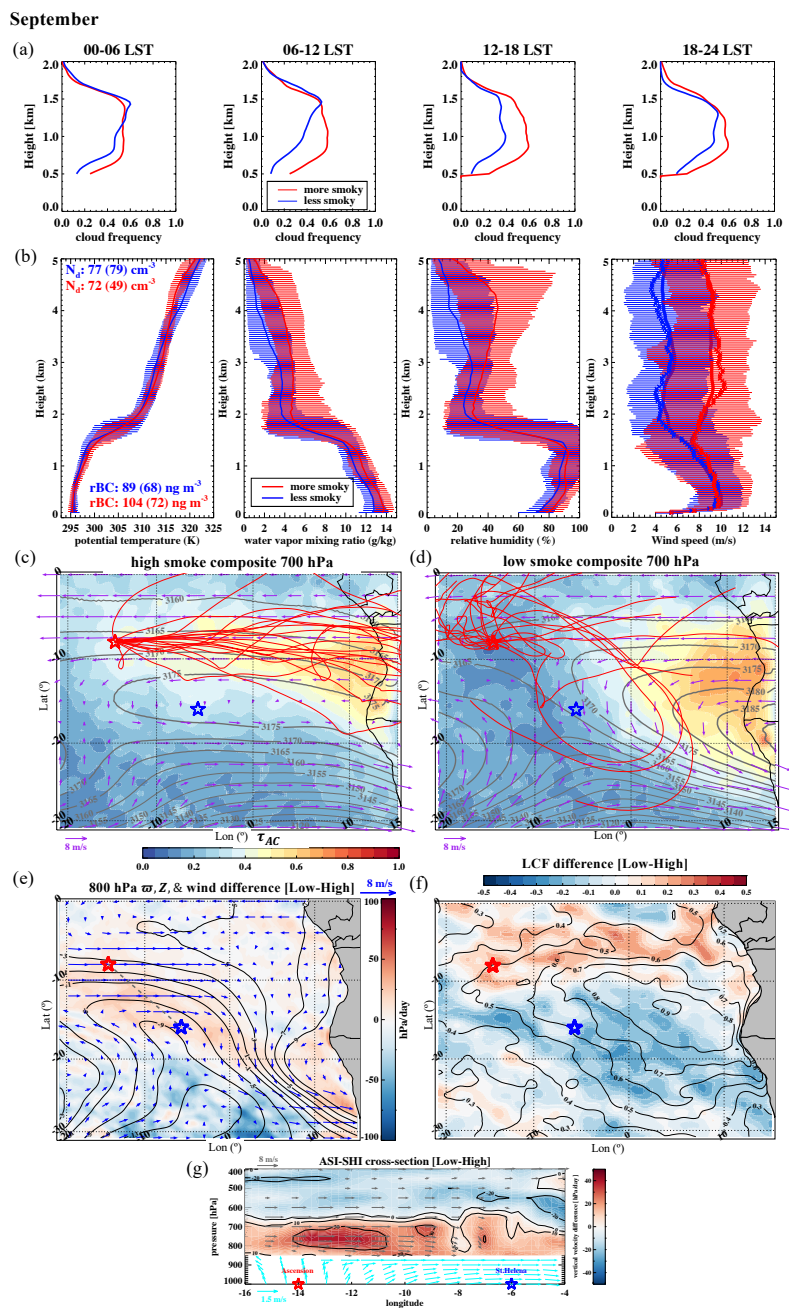
Figure 5. (a) and **(b)** as in Fig. 4a and 4e, but for September, composite-mean (-median) rBC mass concentrations are added on the left panel of **(b)**. **(c)** and **(d)**: HYSPLIT 7-day back trajectories initialized at 2 km over Ascension at noon for September (red spaghetti lines) for days with **(c)** more and **(d)** less smoke, overlaid on composite-mean τ_{AC} (colored contours), 700 hPa ERA5 geopotential heights (m, grey contours) and winds (purple vectors). **(e)** Difference (low-high smoke composite) in 800 hPa geopotential heights (m, black countours), winds (blue vectors) and vertical velocity (hPa day^{-1}, colored background). **(f)** Difference in MODIS daily liquid cloud fraction (LCF; filled-contours, low smoke minus high smoke), overlaid with September-mean LCF (black contours). **(g)** Height cross-section of the vertical velocity difference (low-high smoke days) (colored background) and zonal/meridional winds (vectors; differences < 2 m s^{-1} in the free-troposphere are omitted) between St. Helena and Ascension (red and blue stars respectively in panels **c-g**).

September
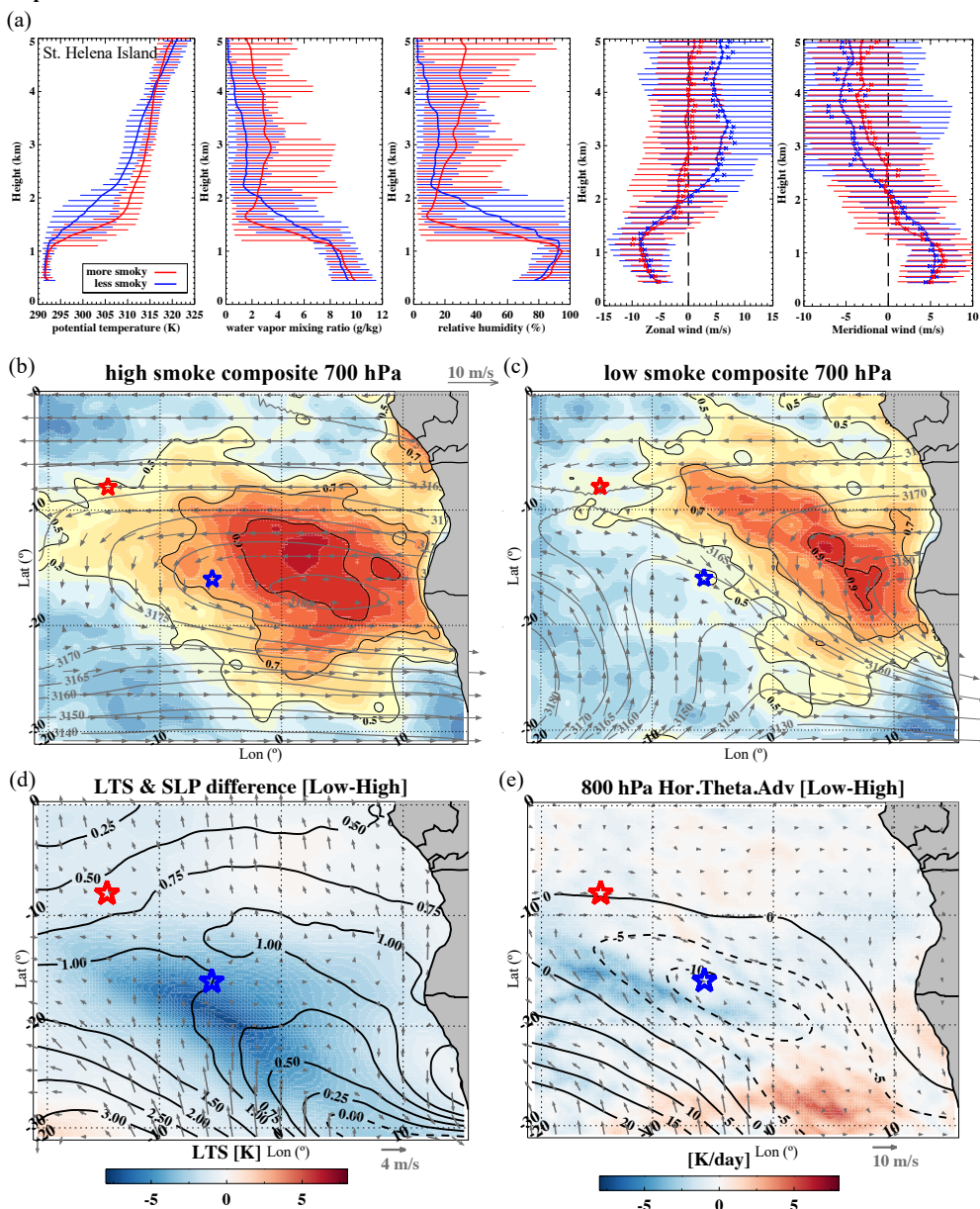
Figure 6. (a) Similar to Fig. 5b, but for St. Helena from 2 days prior to those with high and low smoke loadings at Ascension. Zonal and meridional components of the winds are shown instead of wind speed. **(b)** and **(c)** Corresponding composite-mean MODIS daily liquid cloud fraction (colored contours), 700 hPa ERA5 geopotential heights (m, gray contours) and winds (gray vectors). **(d)** Difference (low-high) in composite-mean lower tropospheric stability (LTS; defined as θ_{800hPa} - $\theta_{1000hPa}$, colored contours), sea level pressure (SLP; hPa, black contours), and 10-m winds (gray vectors). **(e)** Difference (low-high) in 800 hPa composite-mean horizontal temperature advection (colored contours), geopotential heights (m, black contours) and winds (gray vectors). Locations of Ascension and St. Helena indicated in red and blue stars respectively in panels **b-e**.
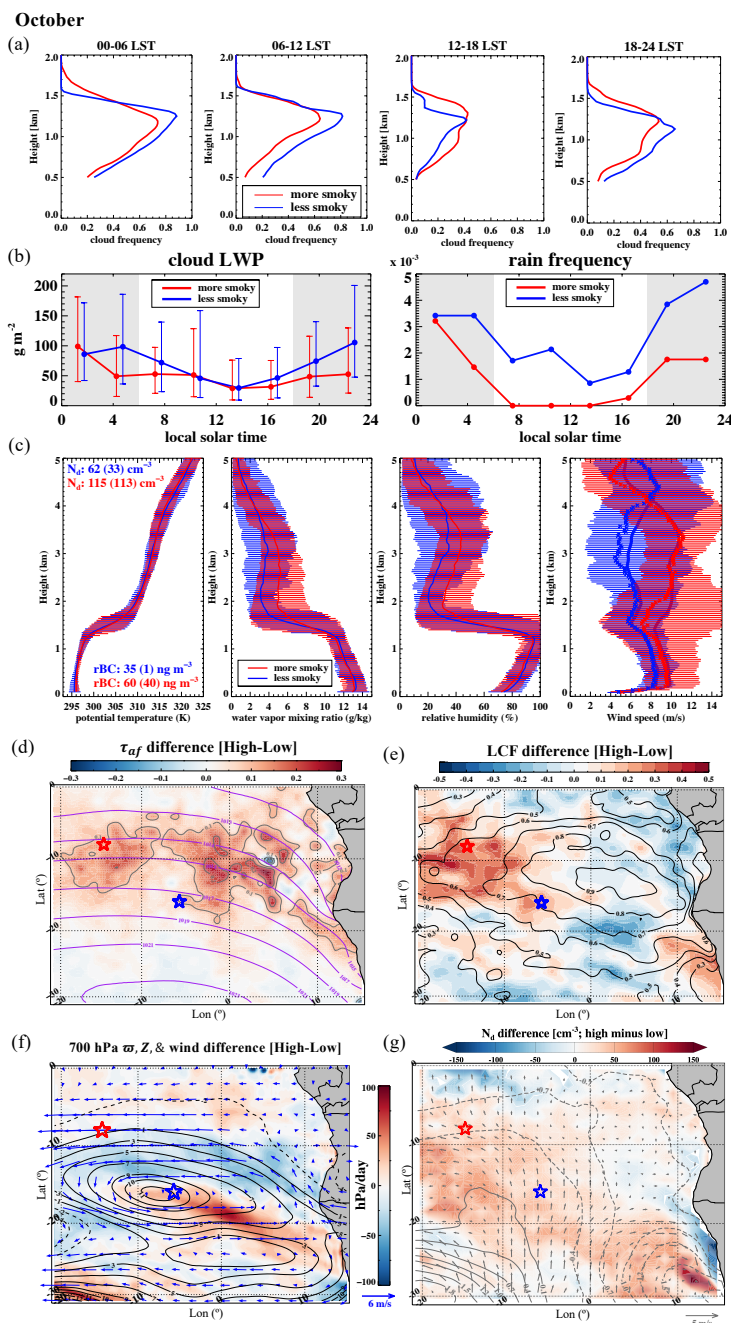
Figure 7. (a) as in Fig. 5a, but for October 2016 only. **(b)** as in 4b and 4c, but for October (2016 and 2017 combined), 3-hour rain frequencies are derived from the tipping bucket instead of the the disdrometer. **(c)** as in Fig. 5b, but for October (2016 and 2017 combined). Difference (high smoke minus low smoke) in October (2016 and 2017 combined) **(d)** MODIS daily τ_{af} (color-filled contours), overlaid with October-mean sea level pressure (hPa, purple), **(e)** MODIS daily liquid cloud fraction (LCF; color-filled contours), overlaid with October-mean LCF (black), **(f)** ERA5 geopotential heights (m, black contours), subsidence (color-filled contours), and horizontal winds (blue vectors) at 700 hPa, and **(g)** daily MODIS-Meyer N_d, overlaid on differences in sea level pressure (hPa, gray contours) and 10-m winds (gray vectors). Ascension Island and St. Helena Island locations indicated with red and blue stars respectively in panels **d-g**.
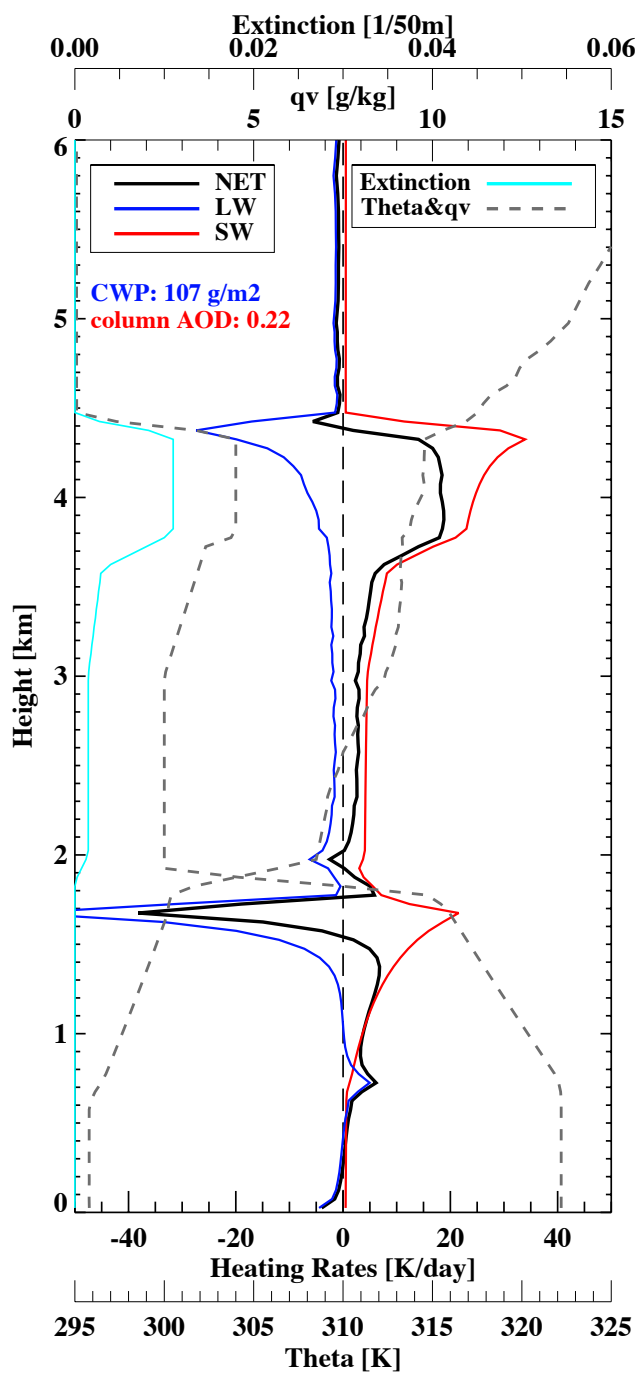
Figure 8. Calculated instantaneous shortwave (red), longwave (blue), and net (black) heating rate profiles at noon on 09/02/2017. θ and q_v profiles from the noon sounding (dashed gray), and the MPL-derived extinction profile (cyan; following Delgadillo et al., 2018) are overlaid. Corresponding τ_a and cloud water path are indicated.